

# We are IntechOpen, the world's leading publisher of Open Access books Built by scientists, for scientists

6,900

Open access books available

185,000

International authors and editors

200M

Downloads

Our authors are among the

154

Countries delivered to

TOP 1%

most cited scientists

12.2%

Contributors from top 500 universities



WEB OF SCIENCE™

Selection of our books indexed in the Book Citation Index  
in Web of Science™ Core Collection (BKCI)

Interested in publishing with us?  
Contact [book.department@intechopen.com](mailto:book.department@intechopen.com)

Numbers displayed above are based on latest data collected.  
For more information visit [www.intechopen.com](http://www.intechopen.com)



# Synchrotron Radiation-Based Quasi-Elastic Scattering Using Mössbauer Gamma Ray with neV-Energy Resolution

*Makina Saito, Toshiji Kanaya and Ryo Mashita*

## Abstract

Gamma rays of energy 14.4 keV from excited  $^{57}\text{Fe}$  nuclei show a very narrow energy width of 4.67 neV by the Mössbauer effect. Mössbauer gamma rays are utilised as probe beams in unique quasi-elastic scattering spectroscopy with neV-energy resolution. The technique enables measurements of atomic/molecular dynamics on timescales between nanoseconds and microseconds for various condensed matter systems, such as supercooled liquids, glasses and soft materials. The microscopic dynamics is measured in time domain or energy domain based on synchrotron radiation using a time-domain interferometer or a nuclear Bragg monochromator, respectively. We introduce state-of-the-art spectroscopic techniques, application results and future perspectives of quasi-elastic Mössbauer gamma ray scattering based on synchrotron radiation.

**Keywords:** Mössbauer gamma ray, synchrotron radiation, quasi-elastic scattering, glass transition, slow dynamics

## 1. Introduction

The recoilless nuclear excitation of a gamma ray and its reversal process of recoilless gamma ray emission were first reported by Mössbauer [1]. These phenomena occur in solids when the recoil momentum of gamma rays in absorption and emission processes is taken up by the whole crystal. Consistently, this physical phenomenon is referred to as the Mössbauer effect [2]. For  $^{57}\text{Fe}$  nuclei, the excitation energy to the first excited state is 14.4 keV, whereas the uncertainty width of the excited state  $\Gamma_0 \sim 4.67$  neV is relatively very narrow. Therefore, the gamma rays emitted from the excited  $^{57}\text{Fe}$  nuclei by the Mössbauer effect show an energy  $E_0 \sim 14.4$  keV and a natural energy width  $\Gamma_0 \sim 4.67$  neV. The photon emitted by the nuclei is called the gamma ray because it originates at the nucleus. However, Mössbauer gamma rays have lower energy than gamma rays involved in astronomy physics and are, instead, closer to the energy range of hard X-rays. In this chapter, we refer to such gamma rays as Mössbauer gamma rays. In these cases, the ratio of the gamma rays' energy to the natural energy width reaches  $\Gamma_0/E_0 \sim 10^{-13}$ , indicating that the Mössbauer gamma rays exhibit very high monochromaticity. The surrounding electrons affect nuclear excitation energies through hyperfine

interactions. Therefore, electronic states around the specific Mössbauer nuclei can be selectively studied from the measured nuclear excitation energies via the Mössbauer effect. This spectroscopic technique, known as Mössbauer spectroscopy, has been widely used for more than 40 elements and 70 nuclear species (referred to as the Mössbauer nuclear species) to resolve various challenges in the fields of chemistry, physics, geology and biology [2].

Microscopic dynamics in condensed matter, which do not contain Mössbauer nuclear species, have been studied since the 1960s with Mössbauer gamma rays [3]. In these experiments, the Mössbauer effect is utilised to generate the monochromatic gamma rays from a radioactive isotope (RI) source, and a quasi-elastic scattering experiment is performed for some samples [3]. In this chapter, we refer to the methods as quasi-elastic gamma ray scattering (QEGS) spectroscopy based on conventional nomenclature, such as inelastic/quasi-elastic neutron/X-ray scattering though this method has often been referred to as the Rayleigh-scattering of Mössbauer radiation method. The neV-energy resolution of the gamma rays from  $^{57}\text{Fe}$  nuclei allows the dynamics to be measured on timescales of about 100 ns. However, the measurements require much longer times because gamma rays from RI sources do not have parallel beams with enough brilliance for the QEGS experiment.

Recently, synchrotron radiation (SR)-based QEGS spectroscopic techniques using a  $^{57}\text{Fe}$ -nuclear Bragg monochromator (NBM) [4, 5] and a time-domain interferometer (TDI) of  $^{57}\text{Fe}$  gamma rays [6] have been developed. These methods have enabled much faster measurements of the atomic/molecular dynamics than RI-based QEGS spectroscopy, owing to the high brilliance and directionality of the SR source. To date, alloys, supercooled molecular liquids, polymers, ionic liquid, liquid crystals and polymer nanocomposite systems have been studied by SR-based QEGS spectroscopy.

In this chapter, we consider Mössbauer gamma rays from  $^{57}\text{Fe}$  nuclei because the gamma ray is most frequently used for QEGS spectroscopy. The length scales of the density correlation function currently observable by SR-based QEGS spectroscopy using TDI range from 0.1 to 6 nm, and the fluctuation timescales vary from few nanoseconds to sub-microseconds, as shown in **Figure 1**. The figure demonstrates how QEGS spectroscopy enables us to study density fluctuations, which are quite difficult to study by conventional spectroscopies in the microscopic range. Many unsolved issues are related to these time and length scales, including microscopic activation processes, which are related to the nature of the glass transition, start to occur in glass-forming materials in the time and length scales with cooling.

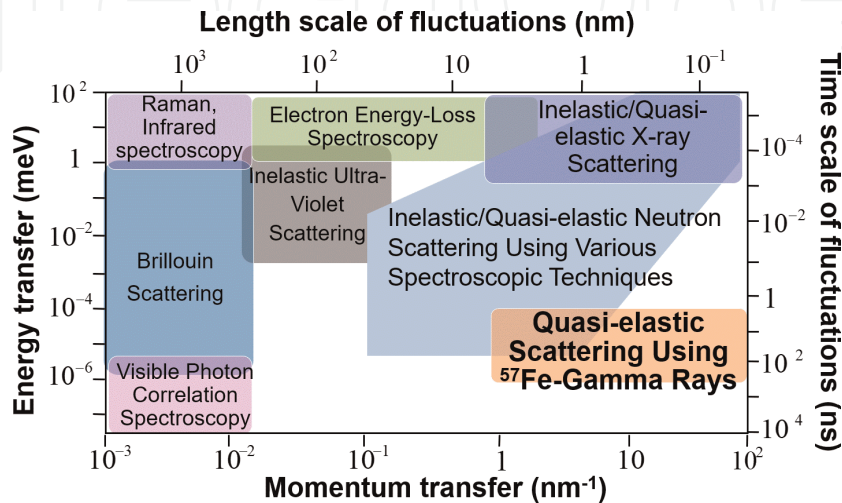


**Figure 1.** Various experimental techniques and the covered time and length scales. Quasi-elastic scattering spectroscopy using gamma rays from  $^{57}\text{Fe}$  covers a unique time- and length-scale region.

This chapter is organised as follows: In section 2, basic concepts of quasi-elastic scattering are introduced, and QEGS spectroscopic techniques are explained. In section 3, experimental results of application studies on several supercooled glass formers are described. In section 4, we conclude this chapter by describing future perspectives of QEGS.

## 2. Quasi-elastic scattering spectroscopy using Mössbauer gamma rays

In this section, we introduce the quasi-elastic scattering technique using Mössbauer gamma rays. In section 2.1, basic concepts of the quasi-elastic scattering technique are described. In section 2.2, we introduce energy-domain spectroscopic techniques of QEGS using Mössbauer gamma rays from conventional RI and SR sources. In section 2.3, time-domain measurement techniques of QEGS spectroscopy using single-line and multi-line TDI are described.

### 2.1 Introduction to quasi-elastic scattering

In this scattering process, gamma rays with wavevector  $\mathbf{k}$  are emitted from the excited  $^{57}\text{Fe}$  nuclei by the Mössbauer effect and Mössbauer gamma rays impinge on a sample. The geometry of the resulting Rayleigh-scattering process is shown in **Figure 2**, where  $\mathbf{k}'$  is the wavevector of the scattered gamma rays and  $\mathbf{q} = \mathbf{k}' - \mathbf{k}$  is the transferred momentum vector of the gamma rays to the sample [7]. The electron density field in the sample can be written as  $\rho(\mathbf{r}, t) = \sum_{i=1}^N \delta(\mathbf{r} - \mathbf{r}_i(t))$ , where  $\mathbf{r}$  and  $t$  are the space coordinate and the time, respectively,  $N$  is the molecular number in the sample and  $\mathbf{r}_i$  is the centre position of atom  $i$ . In the momentum transfer (wavenumber) space, the density field  $g(\mathbf{q}, t)$  is written as  $g(\mathbf{q}, t) = \sum_{i=1}^N \exp\{i\mathbf{q} \cdot \mathbf{r}_i(t)\}$ . Due to atomic/molecular motions in the sample, the gamma rays transfer energy to the sample and vice versa. In quasi-elastic scattering processes, a neV-energy broadening of the gamma rays energy is observed, as shown in **Figure 2**. This peak broadening is due to energy transfers that occur at neV-energies, which are thus much smaller than the incident gamma rays' energy, for which we can thus assume  $|\mathbf{k}| \sim |\mathbf{k}'|$ . Consequently, the amplitude of the transferred momentum is  $q = 2|\mathbf{k}| \sin(\theta)$ , where  $2\theta$  is the scattering angle. When the sample shows disordered structures, as in liquids and glasses, the relevant variable is the absolute value  $q$  rather than the vector  $\mathbf{q}$ .

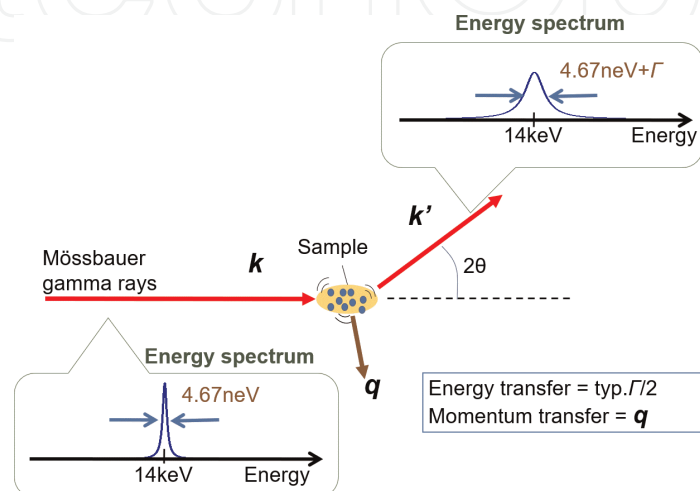


**Figure 2.**  
 Schematic picture of the quasi-elastic scattering process of Mössbauer gamma rays from a sample.



We introduce the spatial correlation function of the electron density  $G(\mathbf{r})$  as  $G(\mathbf{r}) = \langle \rho(\mathbf{r}_0 + \mathbf{r}, t_0) \rho(\mathbf{r}_0, t_0) \rangle$ , where  $\langle \dots \rangle$  denotes the equilibrium average over  $t_0$  and position  $\mathbf{r}_0$ , and  $\mathbf{r}$  is a distance. The static structure factor  $S(\mathbf{q})$  is defined as its space Fourier transform  $S(\mathbf{q}) = \int G(\mathbf{r}) \exp(i\mathbf{q} \cdot \mathbf{r}) d\mathbf{r}$ . For simple monoatomic liquids, the scattering intensity  $I(q)$  is related to  $S(q)$  as  $I(q) = N S(q)$ . From this definition, it appears that the scattering at a given  $q$  is mainly caused by atomic pair correlations roughly occurring over distances  $2\pi/q$ , in a very simple picture. At atomic scales,  $S(q)$  is obtained via X-ray and neutron diffraction experiments.

We introduce the time and space correlation function  $G(\mathbf{r}, t) = \langle \rho(\mathbf{r}_0 + \mathbf{r}, t_0 + t) \rho(\mathbf{r}_0, t_0) \rangle$  describing the microscopic structural dynamics. Its  $q$ -domain representation, often called the intermediate scattering function, is  $S(\mathbf{q}, t) = \int G(\mathbf{r}, t) \exp(i\mathbf{q} \cdot \mathbf{r}) d\mathbf{r}$  and can be measured by neutron spin echo spectroscopy and photon correlation spectroscopy. The spectral intensity of the scattered gamma rays at a given  $q$  is  $I(q, E) = N S(q, E)$ , where  $S(q, E) = \int G(\mathbf{r}, t) \exp[i(\mathbf{q} \cdot \mathbf{r} - tE/\hbar)] dt d\mathbf{r}$  is called the dynamics structure factor. Inelastic/quasi-elastic X-ray scattering using meV-high energy resolution monochromators and neutron scattering using triple-axis spectrometers measure  $S(q, E)$ . Both  $S(q, E)$  and  $S(q, t)$  show quantitatively equivalent information for  $G(\mathbf{r}, t)$ .

## 2.2 Energy-domain spectroscopy of QEGS

In this section, we consider QEGS-based energy-domain spectroscopic techniques using Mössbauer gamma rays from conventional RI and SR sources. **Figure 3a** shows the common experimental design of the technique [8, 9]. In the setup, monochromatic Mössbauer gamma rays impinge on the sample. The quasi-elastic broadening of the scattered gamma ray's energy is analysed by the  $^{57}\text{Fe}$ -Mössbauer absorber, as explained below. As **Figure 3b** shows,  $S(q, E)$  is observed as a transmittance-type spectrum  $I(q, E)$ , which is conceptually written as  $I(q, E) \propto 1 - \int dE' S(q, E') R(E - E')$ , where  $R(E)$  is the resolution function.

### 2.2.1 RI-based QEGS spectroscopy: Rayleigh-scattering Mössbauer radiation

Rayleigh-scattering Mössbauer radiation (RSMR) spectroscopy is a conventional QEGS spectroscopic technique that uses RI as the source of the gamma ray probe. RSMR spectroscopy has been used to study microscopic dynamics in glass formers, proteins and liquid crystals as summarised in a review by Champeney [8]. In this method, monochromatic Mössbauer gamma rays (e.g., from a radioactive  $^{57}\text{Co}$  source with an energy  $E_0$  of 14.4 keV and an energy width of 4.67 neV) are sent to the sample. A broadening of the energy width of the quasi-elastically scattered

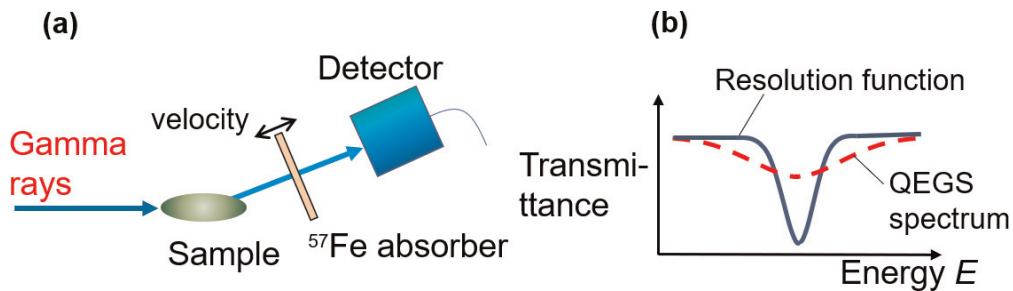


**Figure 3.** Energy-domain QEGS experimental setup and typical spectrum. (a) Schematic figures of QEGS experimental setups for energy-domain measurement and (b) energy spectra of the resolution function (solid line) and QEGS energy spectra in the presence of measurable dynamics (dashed line).

gamma rays from a sample is detected by an absorption spectroscopy method commonly used in Mössbauer spectroscopy (**Figure 3a**). A transmittance-type energy spectrum is obtained by scanning the velocity  $v$  of a movable  $^{57}\text{Fe}$  gamma ray absorber with a single-line excitation profile. The absorber acts as the energy analyser, since its velocity determines the relative energy shift  $E = E_0 v/c$  via the Doppler effect, where  $c$  is the speed of light. RSMR measurements require ample measuring time (at least several weeks) to obtain a spectrum with enough statistics for analysis because the RI source emits gamma rays in all directions, and limited flux is introduced to the sample.

### 2.2.2 SR-based QEGS spectroscopy using $^{57}\text{Fe}$ -nuclear Bragg monochromator

The QEGS-based energy-domain spectroscopic technique using an SR source was developed with the  $^{57}\text{Fe}$ -NBM [4, 5]. NBM is used for a specific condition, in which conventional X-ray diffraction by electrons is forbidden, while nuclear resonant diffraction with nuclear excitation and deexcitation processes is allowed. In such cases, we can detect almost pure Mössbauer gamma rays on a 10 neV-energy width scale due to the specific Bragg angle selectively from a very intense incident SR. Therefore, the SR-NBM system is often called as synchrotron Mössbauer source [10]. The SR-based QEGS experiment has higher efficiency than conventional RSMR using RI because the monochromatic gamma rays from the NBM exhibited high directivity [10]. Moreover, the energy width of the Mössbauer gamma ray probe could be controlled to be much larger than the natural-line width (i.e., up to  $\mu\text{eV}$ ) [11]. This unique characteristic of SR-based QEGS spectroscopy using NBM allows us to measure microscopic dynamics up to sub-nanosecond timescales.

## 2.3 Time-domain measurement of QEGS

The time-domain spectroscopy of QEGS is achieved using TDI. In this section, we introduce time-domain spectroscopic techniques.

### 2.3.1 SR-based QEGS using single-line TDI

The measurement principles of QEGS using the simplest TDI (usually referred to as single-line TDI) are described here. We discuss TDI using Mössbauer gamma rays from  $^{57}\text{Fe}$  because it exhibits the highest utility among nuclear species potentially available for TDI. **Figure 4a** shows the schematic experimental setup [6, 12, 13].

First, we consider the nuclear forward scattering (NFS) case, which often provides a calibration for the QEGS measurement because it is not affected by the dynamics of the sample. In the upper panel of **Figure 4a**, we show the experimental design for the NFS experiment using TDI. The incident SR crosses two identical materials with a single-line  $^{57}\text{Fe}$  nuclear excitation profile corresponding to the nuclear time response function  $G(t)$  ultimately detected by the detector. Most of the SR beam crosses the  $^{57}\text{Fe}$  materials without any interaction. A small portion (typically  $\sim 10^{-6}$ ) of SR excites the  $^{57}\text{Fe}$  nuclei in the materials, causing the gamma rays to emit when the excited  $^{57}\text{Fe}$  nuclei decay. The gamma rays travel undeflected towards the forward detector because of the high directivity inherited from the incident SR. The gamma rays can be distinguished from the much more intense SR because they are delayed from the SR pulse by a typical delay time coincident with the lifetime of the excited  $^{57}\text{Fe}$  nuclei ( $\sim 100$  ns). The upstream material is moved with a constant velocity to change the relative nuclear excitation energy  $\Delta E$  through the Doppler effect and consequently the energy spectrum of the gamma rays at the detector position shows two peaks due to the difference in the gamma ray energy

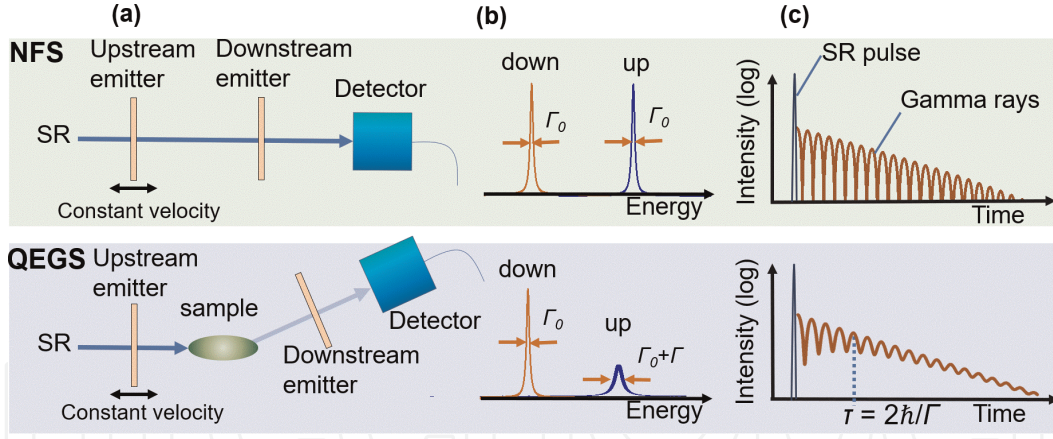


**Figure 4.** NFS and QEGS using single-line gamma rays TDI. (a) Experimental setups and examples of (b) energy spectra and (c) time spectra for NFS and QEGS using single-line TDI.

between the two materials (see the upper panel of **Figure 4b**). The time resolution of the detector is typically 1 ns, which is much shorter than the lifetime of excited  $^{57}\text{Fe}$ , which enables to measure the time spectrum of the delayed gamma rays with high precision. The upper panel of **Figure 4c** shows the corresponding time spectrum. We can see the decay of the gamma rays' intensity on the timescale of excited  $^{57}\text{Fe}$ . On the time spectrum, there is a beating pattern caused by the interference of the gamma rays with two peaks in the energy spectrum.

Next, we consider the QEGS case, corresponding to the scattering of the sample at a finite angle. In the lower panel of **Figure 4a**, we show the QEGS experimental design. The incident SR is scattered by a sample and detected by the detector. Two identical materials with a single-line  $^{57}\text{Fe}$  nuclear excitation profile are placed on the beam path in front of and behind the sample. This system is called the single-line TDI because each material that emits gamma rays (here, referred to as single-line emitter) shows a single-line nuclear excitation profile. A typical energy spectrum of gamma rays at the detector position is shown in the lower panel of **Figure 4b**. The gamma rays from the upstream emitter (denoted as 'up' in **Figure 4b**) are quasi-elastically scattered by the sample and the energy width is broadened as  $\Gamma$ . However, the energy width of the gamma rays from the downstream emitter (denoted as 'down' in **Figure 4b**) is not broadened because it is emitted by the sample after the scattering process.

Next, we considered the time spectrum of the gamma rays obtained by the detector for the QEGS case. When the energy shift is sufficiently large ( $\Delta E \gg \Gamma_0$  and  $\Delta E \gg \Gamma$ ), the radiative coupling effect can be neglected [6, 12, 13]. Additionally, we can assume that the incident SR showed a temporal pulse structure with negligible width. In such cases, the electric field  $E(q, t)$  at detector position at an angle corresponding to  $q$  can be written as

$$E(q, t) \propto \delta(t) + g(q, t)G(t)e^{i\omega_Q t} + g(q, 0)G(t) \quad (1)$$

where  $\omega_Q = \Delta E/\hbar$  is the angular frequency of the beating pattern. We ignored the coefficient of the transmittance because it does not affect the final spectrum shape. The first, second and third terms of Eq. (1) represent the electric field amplitudes of the prompt SR, gamma rays emitted from the upstream and downstream emitters, respectively. The delayed gamma rays' measurement for part of the obtained time spectrum  $I(q, t)$  is written as

$$I(q, t) \propto |G(t)|^2 S(q) [1 + S'(q, t) \cos(\omega_Q t)]. \quad (2)$$



In Eq. (2),  $S'(q, t)$  is the intermediate scattering function normalised by  $S(q)$ , that is,  $S'(q, t) \equiv S(q, t)/S(q)$  and the static structure factor  $S(q)$  is  $S(q) = \langle |g(q, t)|^2 \rangle = \langle |g(q, 0)|^2 \rangle$  [6, 12, 13]. We assume that the scattering from a sample with a macroscopic number of atoms was measured with an acquisition time long enough to provide a reliable determination of the relevant average ensembles. For an NFS experiment under the same emitter conditions, the NFS time spectrum is expressed by Eq. (2) with  $S(q) = 1$  and  $S'(q, t) = 1$ . Examples of time spectra for NFS and QEGS cases with a relaxation time  $\tau$  of 100 ns are shown in the upper and lower panels of **Figure 4c**, respectively. For the actual fitting of the spectra, the time resolution of the detector and constant background noise would need to be considered.

Next, we considered the meaning of the time spectrum. The broadening of the gamma rays by an energy width  $\Gamma$  reflects the dynamics in a sample. The broadening induces the distribution of the beat frequency in a time domain and this effect is seen as the relaxation of the beating pattern with the relaxation time  $\tau = 2\hbar/\Gamma$  in the simplest case. Further consideration revealed that the relaxation time of the beating pattern coincides with the relaxation time of the density correlation in the sample (namely, the intermediate scattering function) [6, 12, 13]. This analysis is a basic interpretation of how the time spectrum reflects the dynamics in a sample. We note that an intrinsic relaxation of  $S'(q, t)$  caused by an external vibration, for example, should also be considered for the actual dynamics study.

### 2.3.2 SR-based QEGS spectroscopy using multi-line TDI

Here, we consider QEGS spectroscopy using multi-line TDI [14]. In this case, emitters with several nuclear excitation energies are used for TDI. We assume again that the two emitters show different excitation energies from each other. Generally, the nuclear time response functions in emitters are different from each other in multi-line cases. Therefore, we introduce the time response functions for the upstream and downstream emitters as  $G_1(t)$  and  $G_2(t)$ , respectively. In such cases, we obtain the expression  $E(q, t)$  as  $E(q, t) \propto \delta(t) + g(q, t)G_1(t) + g(q, 0)G_2(t)$  from Eq. (1). The intensity of the delayed gamma rays can be written as

$$I(q, t) \propto S(q) \left\{ |G_1(t)|^2 + |G_2(t)|^2 + S'(q, t)[G_1^*(t)G_2(t) + G_1(t)G_2^*(t)] \right\}. \quad (3)$$

As an example of multi-line TDI, we considered  $\alpha$ -iron foils as emitters, where the nuclear excitations are allowed for six different energies without an external magnetic field. **Figure 5a** shows an experimental setup using  $\alpha$ -iron emitters. When the magnetic field is applied to the  $\alpha$ -iron foils, as shown in **Figure 5a**, the transitions allowed in the two emitters are selected to be different from each other. Consequently, the gamma rays' energy emitted from these two emitters is different, as shown in **Figure 5b**, where the gamma rays from the upstream and downstream emitters are denoted as 'up' and 'down', respectively. Examples of the energy spectra of gamma rays for cases without atomic motion and motion with a relaxation time of 100 ns are shown. **Figure 5c** depicts the corresponding time spectra. The beating pattern changes following the decay of  $S'(q, t)$ . By introducing the multi-line condition, the interference beating pattern of the gamma rays on the time spectrum becomes more complex than the single-line case. However, the incident SR can be more effectively utilised for experiments and the gamma rays' count rate increases. Additionally, it can be shown that the time spectrum changes more drastically, reflecting the dynamics [14]. These properties of the multi-line TDI greatly improve the measurement efficiency in comparison to the single-line method.



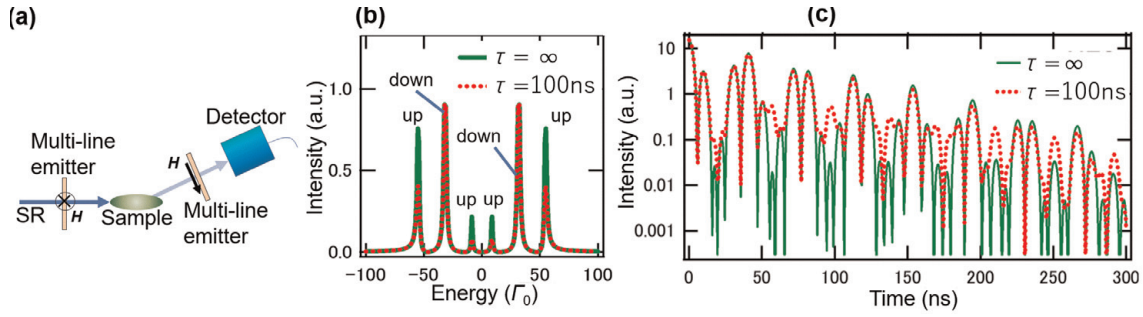


**Figure 5.** Examples of quasi-elastic scattering using multi-line gamma rays TDI. (a) Experimental setup and examples of (b) energy spectra and (c) time spectra in the cases of no relaxation and  $\tau = 100$  ns.

### 2.3.3 SR-based QEGS using TDI considering energy resolution of incident SR

Here, we consider the effect of the energy width of the incident SR on the gamma rays' time spectrum obtained by the QEGS experiment. After the first induced heat load from the Si(111) monochromator, the SR showed a relatively broad energy profile; an energy width of the eV order could be considered white for the QEGS system. However, the incident SR is usually further monochromatised by using a high-resolution monochromator (HRM). This device generates typical energy widths in the meV range to suppress radiation damage to the system [6, 12–14]. The meV-energy interval is equivalent to or smaller than the energy scale of phonons in samples. Therefore, a portion of the incident SR transfers a larger amount of energy to the sample by interacting with the phonons. We found that the inelastic scattering process affects the intensity ratio of the gamma rays from the upstream and downstream emitters. Considering this effect, we modify Eq. (3) as

$$I(q, t) \propto S(q) \left\{ |G_1(t)|^2 + |G_2(t)|^2 + S'(q, t) [G_1^*(t)G_2(t) + G_1(t)G_2^*(t)] - (1 - f_{\Delta E}) |G_2(t)|^2 \right\}, \quad (4)$$

where  $f_{\Delta E}$  is the factor reflecting the sample dynamics on a meV-energy scale [14]. It was confirmed that the QEGS time spectrum obtained using TDI with multi-line gamma rays could be nicely analysed using Eq. (4) [14]. Additionally, we showed that QEGS spectroscopy using HRM originally has two resolution functions on neV- and meV-energy scales. By using multi-line TDI in the condition  $|G_1(t)|^2 \neq |G_2(t)|^2$ , dynamical information, such as the elastic scattering intensity, can be obtained simultaneously on nanosecond and sub picosecond timescales [14].

## 3. Application results of SR-based QEGS using TDI

To date, SR-based QEGS spectroscopy has been used to study glass-forming molecular liquids [15–19], polymers [20], polymer nanocomposites [21], ionic liquids [22], alloys [23] and liquid crystals [24].

### 3.1 Microscopic dynamics in glass formers

The general mechanism of the liquid-glass transition phenomenon, which has not been revealed, has attracted much interest. It is widely accepted that a relaxation process, known as the  $\alpha$  process, is closely related to glass transitions [25–27].

Therefore, atomic and molecular dynamics of supercooled glass formers have been energetically investigated to understand glass transitions. The temperature ( $T$ ) dependencies of the  $\alpha$ -relaxation time and viscosity of some glass formers show super-Arrhenius behaviour when cooled towards the glass transition temperature [28]. These behaviours are often fitted by the Vogel-Fulcher-Tammann (VFT) law:  $\eta(T), \tau(T) \propto \exp [DT_0/(T - T_0)]$ , where  $D$  is the fragility index and  $T_0$  is the Vogel-Fulcher temperature [25–27]. The slope of this super-Arrhenius behaviour is determined by the fragility index and its physical origin still has not been fully elucidated; this limitation remains one of the central challenges in studying glass transitions.

The other challenging task in these systems is understanding the origin of the dynamical change of the  $\alpha$  process, which starts to occur at a temperature of  $\sim 1.2 T_g$  upon cooling, where  $T_g$  is the glass transition temperature. The changing temperature is recognised as the dynamical crossover temperature  $T_c$  [29]. In addition to the  $\alpha$  process, various processes have been observed in relaxation maps, which summarise the temperature dependence of processes in glass formers. Among the various relaxation processes subjected to a thorough scrutiny, it is worth mentioning the Johari-Goldstein (JG)- $\beta$  process, which emanates from the  $\alpha$  process in relaxation maps and, instead, follows Arrhenius behaviour  $\tau(T) \propto \exp [E_A/(RT)]$  even below the glass transition temperature, where  $E_A$  is the activation energy and  $R$  is the gas constant [30]. Recently, the JG- $\beta$  process was believed to commonly exist in supercooled glass formers and relate to the nature of the glass transition mechanism [27]. The branching temperature of the JG- $\beta$  process from the  $\alpha$  process  $T_{\alpha\beta}$  is frequently seen near the dynamical crossover temperature  $T_c$ . This synchronism is believed to be an intrinsic feature of supercooled glass formers. However, the dynamical crossover and branching phenomena are far from being understood fully. Conventional methods, such as dielectric relaxation spectroscopy, do not provide spatial-scale information on the dynamics, and the  $\alpha$  and JG- $\beta$  processes are not clearly discerned around  $T_c$  and  $T_{\alpha\beta}$ . Therefore,  $T_{\alpha\beta}$  has been estimated as a crossing point of the  $\alpha$ -relaxation time and an extension of the JG- $\beta$  relaxation time by assuming the Arrhenius law [27].

Understanding the microscopic dynamics around  $T_c$  and  $T_{\alpha\beta}$  is indispensable to elucidating the glass transition mechanism. SR-based QEGS spectroscopy is a method ideally suited to understand the microscopic dynamics in deeply supercooled glass formers around  $T_c$  and  $T_{\alpha\beta}$  and its evolution towards the glass transition. This technique enables to measure the atomic/molecular dynamics with specification of its spatial scale on a nanosecond/microsecond timescale, where the JG- $\beta$  process commonly occurs [27]. We performed SR-based QEGS experiments using single-line and multi-line TDI on various glass formers. We introduce the results on *o*-terphenyl in section 3.2 and polybutadiene in section 3.3. Additionally, the application results of a polymer nanocomposite system are discussed in section 3.4.

### 3.2 Results on *o*-terphenyl

*o*-terphenyl (OTP) is widely studied as a model system of glass formers. For deeply supercooled OTP, it has been reported that a change in the VFT parameters of the  $\alpha$ -relaxation timescale occurs at around 290 K [31]. Additionally, decoupling of the rotational and translational diffusion coefficients of the tracer molecules [32], an abrupt decrease of the stretching parameter of the  $\alpha$ -relaxation form [33] and formation of a cusp in the temperature dependence of  $f_{DW}$  [34] have been reported at 290 K upon cooling. From these observations, 290 K can be recognised as the dynamical crossover temperature  $T_c$ . Additionally, dielectric relaxation spectroscopy

studies have revealed that the branching temperature  $T_{\alpha\beta} \sim 290$  K is almost the same as  $T_c$  for OTP [35]. Again,  $T_{\alpha\beta}$  should be carefully interpreted because it was estimated by the extrapolation assumption whose validity has not been confirmed. Moreover, the details of the branching phenomenon of the  $\alpha$  and JG- $\beta$  processes and the relationship between  $T_{\alpha\beta}$  and  $T_c$  are still unclear.

We studied OTP using single-line  $^{57}\text{Fe}$  gamma rays TDI for the QEGS measurements [16, 20]. Detectors were placed at angles corresponding to  $q$  values shown in the inset of **Figure 6**. For analysing the time spectra, we applied Eq. (2) assuming the Kohlrausch-Williams-Watts (KWW) function  $f \exp \left[ -(t/\tau)^{\beta_{\text{KWW}}} \right]$  for the relaxation of  $S'(q, t)$ , where  $f$  is the amplitude of the relaxation,  $\tau$  is the relaxation time, and  $\beta_{\text{KWW}}$  is the stretching parameter. In the obtained QEGS time spectra, the values of  $\beta_{\text{KWW}}$  were determined to be  $0.56 (\pm 0.31)$  for  $q$  values ranging from 27 to  $50 \text{ nm}^{-1}$  (265 K),  $0.64 (\pm 0.15)$  for  $14 \text{ nm}^{-1}$  (285 K) and  $0.66 (\pm 0.25)$  for  $16$ – $31 \text{ nm}^{-1}$  (285 K) [16]. Therefore, we analysed all QEGS time spectra by using a fixed  $\beta_{\text{KWW}}$  of 0.6 [34]. The  $\tau$  obtained by fitting was transformed to a mean relaxation time  $\langle \tau \rangle$  using the equation  $\langle \tau \rangle = \tau \Gamma(1/\beta_{\text{KWW}})/\beta_{\text{KWW}}$ , where  $\Gamma$  is the gamma function. In **Figure 6**, we show the obtained relaxation map with spatial-scale information of the dynamics as a  $q$  dependence.

**Figure 6** depicts the temperature dependence of  $\langle \tau \rangle$ . At  $q = 14 \text{ nm}^{-1}$ , the temperature dependence obeys the VFT law, as suggested by the comparison with best-fitting curve obtained by the least-squares method. The best-fitting VFT parameters were determined to be  $D = 3.1 (\pm 0.3)$  and  $T_0 = 235 (\pm 26)$  K. We confirmed that the obtained  $\langle \tau \rangle$  values are consistent with reported  $\alpha$ -relaxation times [35]. This agreement suggests that the relaxation observed at  $q = 14 \text{ nm}^{-1}$  is caused by the  $\alpha$  process.

In the larger  $q$  region ( $18 < q < 42 \text{ nm}^{-1}$ ), the temperature dependencies of  $\langle \tau \rangle$  were found to obey the VFT law above 278 K, as shown in **Figure 6**; however, these data follow the Arrhenius law below 278 K ( $1000/T \sim 3.6 \text{ K}^{-1}$ ). The turning temperature of 278 K appears to be independent of  $q$  within experimental error. The obtained  $\langle \tau \rangle$  values at  $q = 18 \text{ nm}^{-1}$  are similar to the JG- $\beta$  relaxation times obtained by dielectric relaxation spectroscopy (shown as a dashed line in **Figure 6**) [31]. Further consideration revealed that the relaxations observed at the large  $q$  region

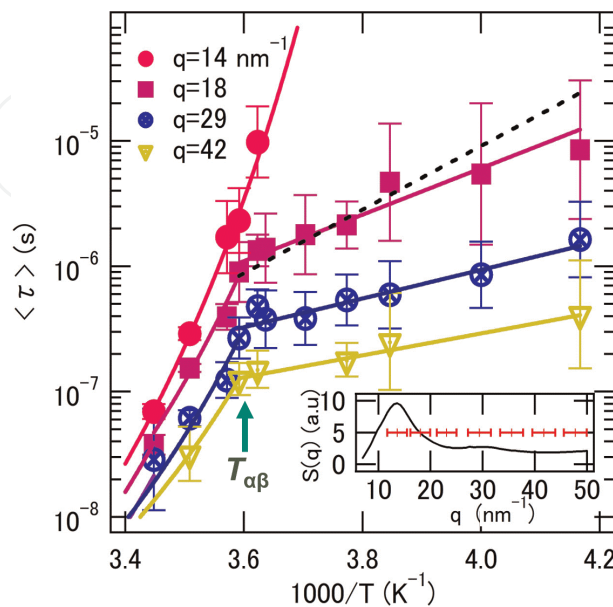


**Figure 6.** Temperature dependence of  $\langle \tau \rangle$  at typical  $q$  values. The solid lines are curves fitted by the Arrhenius and VFT laws. The inset shows  $S(q)$  and corresponding  $q$  values of the measurement. The dashed line shows the JG- $\beta$  relaxation time obtained by dielectric relaxation spectroscopy.



below 278 K are mainly caused by the JG- $\beta$  process [16]. Since the  $T$  dependence of  $\langle\tau\rangle$  above 278 K at  $q = 14 \text{ nm}^{-1}$  is similar to the one observed at larger  $q$  values, we deduce that above 278 K,  $\alpha$ -relaxations dominate. Therefore, the temperature of 278 K can be identified as the branching temperature  $T_{\alpha\beta}$ , at which, at sufficiently large  $q$ 's, the main relaxation changes from the  $\alpha$  to JG- $\beta$  type upon cooling. Furthermore, since JG- $\beta$  emerges only at large  $q$  values ( $18 < q < 42 \text{ nm}^{-1}$ ), these have a mainly local character [36–38]. The obtained branching temperature  $T_{\alpha\beta} \sim 278 \text{ K}$  is clearly different from the one,  $T_{\alpha\beta} \sim 290 \text{ K}$ , previously obtained from the extrapolation of the JG- $\beta$  relaxation time. This discrepancy suggests that this extrapolation method is not appropriate as also shown in Ref. [16]. Additionally, we found a clear correlation in which:  $T_c \sim 290 \text{ K} > T_{\alpha\beta} \sim 278 \text{ K}$ . This relation suggests that the branching of the JG- $\beta$  process requires further cooling from the onset temperature of the  $\alpha$  process dynamical change, which is in contrast to previous reports.

### 3.3 Results on polybutadiene

As mentioned in section 3.2, the nature of glass transition is still not fully understood despite thorough investigative efforts [39]. In the last three decades, extensive studies on glass transitions have been performed theoretically, experimentally and by computer simulations. One of the most important experimental results constructed relaxation time maps of several glass-forming materials [35] by predicting the decoupling of the JG- $\beta$  process from the  $\alpha$  process. Extensive experimental studies have been performed to reveal the decoupling mechanism using various techniques such as NMR [40], dielectric relaxation (DR) [41] and neutron spin echo (NSE) [42–44]. We performed QEGS measurements using single-line TDI on polybutadiene (PB), which is a typical glass-forming polymer, to decouple the JG- $\beta$  process from the  $\alpha$  process [20].

The sample used in this experiment was 1,4-cis-trans-polybutadiene (PB), which is never crystallised because of the microstructure of cis:trans:vinyl = 47:46:7. The  $T_g$  determined by differential scanning calorimetry (DSC) was 170 K. The same QEGS measurements were performed on PB as OTP, and the observed time spectra were analysed in the same manner as OTP using Eq. (2). In the analyses, we employed a stretched exponential function with an exponent  $\beta_{\text{KWW}}$  of 0.45 as an intermediate scattering function [42–44].

The average relaxation time  $\langle\tau_{\text{KWW}}\rangle$  obtained from the fitting curve is shown in **Figure 7** as a function of the inverse of absolute temperature  $1/T$  at  $q = 9.6, 15, 21, 27, 32$  and  $39 \text{ nm}^{-1}$ . The average relaxation times  $\langle\tau_{\text{KWW}}\rangle$  evaluated from the fitting curve are consistent with those reported in the literature [20, 40–44]. The viscosity timescale  $\tau_\eta(T)$  of PB is shown as a thick dashed line in **Figure 7**. This timescale was derived from the viscosity of the polymer melts via the Rouse model, which connects the viscosity  $\eta$  with the monomeric friction coefficient  $\zeta$  through  $\tau_\eta(T) \sim \zeta(T)/T$  [43]. The temperature dependence here is described by the VFT law. The temperature of  $\langle\tau_{\text{KWW}}\rangle$  at  $q = 9.6$  and  $15 \text{ nm}^{-1}$ , that is, slightly below and at the first peak in  $S(q)$ , shows very similar temperature dependence (the VFT law) to the viscosity timescale  $\tau_\eta(T)$ . Therefore, the VFT law was fitted to the observed  $\langle\tau_{\text{KWW}}\rangle$  at  $q = 9.6$  and  $15 \text{ nm}^{-1}$ . The lines in the figure are the results of the fits at various  $q$  values. The fact that the relaxation times observed at  $q = 9.6$  and  $15 \text{ nm}^{-1}$  follow the same temperature dependencies as the viscosity timescale suggests that  $\langle\tau_{\text{KWW}}\rangle$  at  $9.6$  and  $15 \text{ nm}^{-1}$  is dominated by the  $\alpha$  process. On the other hand, the temperature dependencies of  $\langle\tau_{\text{KWW}}\rangle$  at  $q = 21, 27, 32$  and  $39 \text{ nm}^{-1}$  above the valley in  $S(q)$  are very different from those at  $9.6$  and  $15 \text{ nm}^{-1}$ . At temperatures above  $\sim 210 \text{ K}$  ( $T_{\alpha\beta}$ ), it follows the VFT law, whereas it changes to Arrhenius behaviour



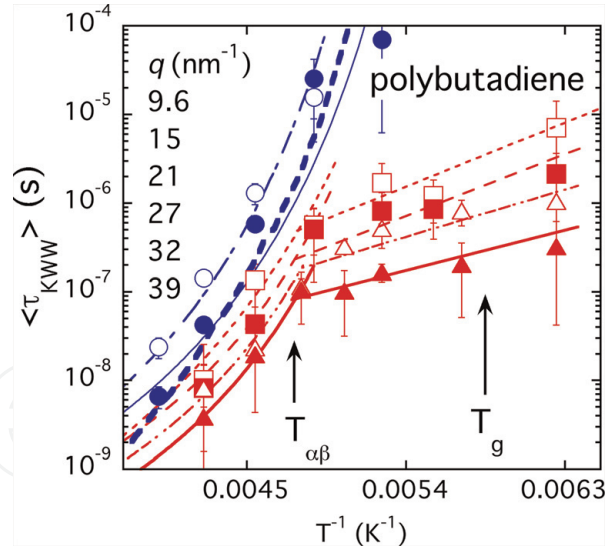


**Figure 7.**

Temperature dependence of the mean relaxation time  $\langle \tau_{\text{KWW}} \rangle$  obtained for PB at  $q = 9.6$  ( $\circ$ , chain line), 15 ( $\bullet$ , thin solid line), 21 ( $\square$ , dotted line), 27 ( $\blacksquare$ , dashed line), 32 ( $\triangle$ , two-dot chain line) and 39 ( $\blacktriangle$ , thick solid line) nm and fitting curves given by symbols and lines, respectively. Thick dashed line represents temperature dependence of viscosity timescale  $\tau_{\eta}(T)$ .

below  $T_{\alpha\beta}$ . Here  $T_{\alpha\beta}$  denotes the transition temperature. Therefore, the VFT law was used to fit data above  $T_{\alpha\beta}$  at each  $q$ , whereas the Arrhenius equation was used for data below  $T_{\alpha\beta}$ . We thus conclude that the  $\alpha$  process occurs above  $T_{\alpha\beta}$ , as suggested by the corresponding VFT behaviour, and it changes to the JG- $\beta$  process below  $T_{\alpha\beta}$ , similar to what was observed in OTP. The observation here that the  $\alpha$  process changes to the JG- $\beta$  process at  $T_{\alpha\beta}$  above the first peak in  $S(q)$  contradicts the NSE results on PB [44] where no transition was observed in the high  $q$  range. It should be emphasised that this new transition finding at the higher  $q$  range can be attributed to the appropriate time and spatial resolutions of the SR-based QEGS technique for observing the branching phenomenon.

An extended mode coupling theory (eMCT) has been proposed to account for hopping processes [45]. This theory predicts a dynamical transition from the  $\alpha$  process to a local, hopping-dominated, relaxation process at  $T_c$ . In other words, this transition corresponds to the switch of the temperature dependence from the VFT law to the Arrhenius law. In the eMCT framework, the transition from the  $\alpha$  process to the JG- $\beta$  process corresponds to the transition from the hydrodynamic continuous motion to the hopping motion. The fact that the transition above the first peak occurs near  $T_c$  supports this interpretation. In the present experiment, however, we observed that the  $\alpha$  process persisted even below  $T_{\alpha\beta}$  ( $\sim T_c$ ) near the first  $S(q)$  peak. In other words, no transition occurred near the first peak. In this sense, the eMCT cannot be directly applied to our results.

The question still remains as to why the  $\alpha$  process lasts even below  $T_{\alpha\beta}$  at the first peak. Richter et al. have intensively studied relaxation processes in PB using NSE [42, 43] and found that the  $\alpha$  process was observed at the first peak in  $S(q)$ , whereas the JG- $\beta$  process was observed at the valley in  $S(q)$  as mentioned above. These results agree with our observations below  $T_{\alpha\beta}$ . The key point of their results is that the intermolecular interaction is very important for understanding the transition. It has been demonstrated that the first peak in  $S(q)$ , the intermolecular correlation, is the strongest, leading to cooperative motion. However, at the valley, the intermolecular correlations are weaker than the first peak, and molecules move less cooperatively or freely. Hence, the cooperative  $\alpha$  process is dominant at the first peak, and the isolated motion or the slow JG- $\beta$  process is dominant at the valley. According to the eMCT, the  $\alpha$ -relaxation changes to the JG- $\beta$  one (hopping process)

at around  $T_c$  even at the first peak of  $S(q)$ ; however, in our experiment, the  $\alpha$  process was still observed below  $T_c$  ( $\sim T_{\alpha\beta}$ ) at the first peak. This discrepancy must be due to the strong cooperativity of the relaxation over distances roughly corresponding to the first  $S(q)$  peak, which was not included in the eMCT.

### 3.4 Results on polybutadiene with nano-silica

Tyre rubber has been continuously developed to improve various aspects of its performance, such as its grip, fuel consumption and wear resistance, by adding fillers such as silica nanoparticles and cross-linking agents [46, 47]. However, the microscopic mechanisms behind these improvements are still not fully elucidated and a better understanding is needed to further improve tyre products. Many studies have shown that confined polymer layers around nanoparticles affect the rubber's macroscopic properties [48–57]. Molecular-scale dynamics studies have also revealed that the presence of nanoparticles slows down the microscopic segmental  $\alpha$ -relaxation motion and increases its heterogeneity [52, 53]. However, we still do not have a complete picture of the microscopic dynamics for these systems. Additionally, the effect of the particle size on the microscopic dynamics has not been elucidated.

To elucidate the effect of nanoparticles on the microscopic  $\alpha$ -relaxation dynamics of polymers, we studied the microscopic dynamics of a polybutadiene (PB) and silica nanoparticle mixture by SR-based QEGS using multi-line TDI. Two types of samples were used for this experiment: pure 1,4-PB and 1,4-PB nanocomposites with silica nanoparticles. Two PB nanocomposites, PB-silica20 and PB-silica100, were prepared with 20 vol% of silica nanoparticles with average diameters of 20 and 100 nm, respectively. The glass transition temperature  $T_g$  of pure PB was determined to be  $\sim 180$  K and no  $T_g$  difference could be detected among the three samples.

**Figure 8** shows the obtained wide-angle X-ray scattering (WAXS) profile of the two nanoparticle samples. From these WAXS results, we confirmed that the position of the main peak, mainly reflecting the intermolecular correlation of the PB, had changed very little and was covered by the  $q$  region in the quasi-elastic scattering measurements (see the bar in the figure). Least-squares fits were performed for the obtained PB time spectrum using Eq. (4) modelling the normalised intermediate scattering function with a KWW profile. The value of  $\beta_{\text{KWW}}$  for pure PB was determined to be  $0.48 \pm 0.10$  at  $q \sim 14 \text{ nm}^{-1}$ , which is consistent with the previously reported  $\beta_{\text{KWW}}$  value of 0.45 [42]. We obtained  $\tau$  by setting  $\beta_{\text{KWW}}$  to be 0.45 for the pure PB spectra and then calculated the mean relaxation time  $\langle \tau \rangle$  from  $\langle \tau \rangle = \tau \Gamma(1/\beta_{\text{KWW}})/\beta_{\text{KWW}}$ , where  $\Gamma$  is the gamma function [42].

Next, for the PB nanocomposites with silica nanoparticles, the polymer dynamics was studied through the analysis of the relaxation time extracted from the intermediate scattering function, while also considering its non-relaxing component originating from the stable nanoparticles. For the polymer nanocomposite systems, it is known that the contribution of the  $\alpha$ -relaxation of polymers to the intermediate scattering function can be treated as a KWW function [48, 49]. Therefore, we used the function  $F(q, t) = f(q) \exp \left\{ -[t/\tau(q)]^{\beta_{\text{KWW}}(q)} \right\} + c(q)$  to fit the normalised intermediate scattering function for the time spectra of PB-silica100 and PB-silica20, where  $c(q)$  is the contribution of the non-relaxing component. By fitting the time spectra obtained for PB-silica100 at 250 K, we determined that the contribution of the non-relaxing component was  $c = 0.22 \pm 0.07$  at  $q \sim 14 \text{ nm}^{-1}$ , assuming  $\beta_{\text{KWW}} = 0.45$ . We used these values to analyse the time spectra of both PB-silica20 and PB-silica100 because (i) the volume fraction of silica nanoparticles was the

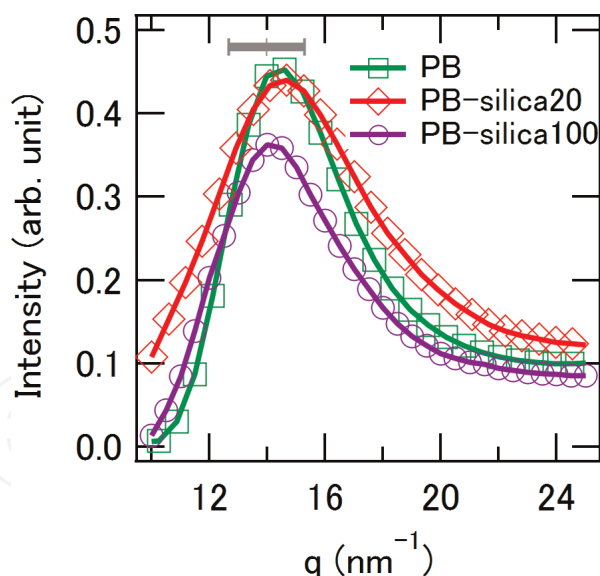


**Figure 8.**

WAXS profile obtained for pure PB and PB-Si100 at room temperature, and for PB-silica20 at 270 K. The bar represents the  $q$  region of the quasi-elastic scattering measurements.

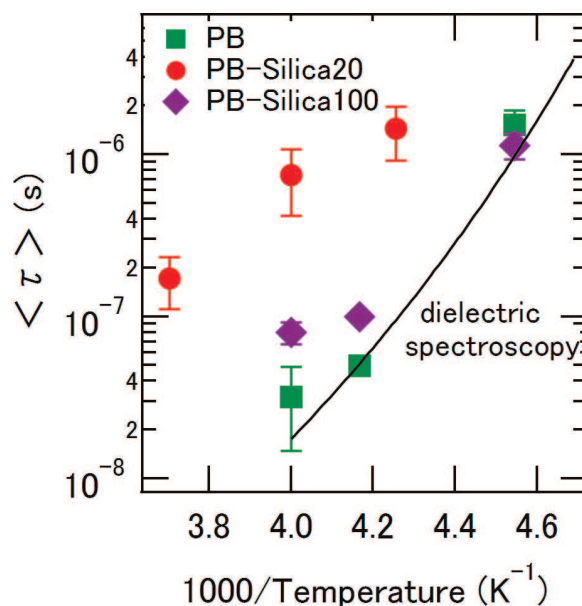


**Figure 9.**

Temperature dependence of the averaged relaxation times obtained for pure PB, PB-silica20 and PB-silica100 at  $q = 14 \text{ nm}^{-1}$ . The error bars indicate the standard deviations, and the line indicates the  $\alpha$ -relaxation times obtained by dielectric relaxation spectroscopy [58].

same for both samples and the  $c$  value could also be assumed to be the same and (ii) the non-relaxing component of the polymer was found to be negligible in a mixture of PB and carbon black nanoparticles in the  $q$  range of the first peak [48, 49].

**Figure 9** shows the temperature dependence obtained for  $\langle \tau \rangle$ . The  $\alpha$ -relaxation times of pure PB obtained by dielectric relaxation spectroscopy (depicted as a line in **Figure 9**) demonstrate that our results are consistent with the dielectric relaxation spectroscopy results [58]. The temperature dependencies of  $\langle \tau \rangle$  obtained for PB-silica20 and PB-silica100 also show divergent behaviour, although the VFT parameters appear to be different compared to pure PB. At 250 K, the  $\alpha$ -relaxation times obtained at  $q = 14 \text{ nm}^{-1}$  for PB-silica20 and PB-silica100 were longer than those for pure PB, and this relation holds true throughout the studied temperature region. These data suggest that the nanoparticles cause the polymer  $\alpha$ -relaxation motion to slow down. Moreover, the dynamics of PB-silica20 were much slower than

PB-silica100. Here, the volume fractions of silica nanoparticles in the PB-silica20 and PB-silica100 nanocomposites were the same, but the PB-silica20 surface area was on average 25 times larger than the PB-silica100 surface area. Therefore, the obtained results suggest that the polymer  $\alpha$ -relaxation dynamics was restricted by contact with the surfaces of the nanoparticles and became even more restricted as the surface area increased. This result is consistent with the conventional idea that the  $\alpha$ -relaxation times of polymers slow down due to interactions (chemical attachment and physical absorption) between the polymer and the silica nanoparticles on the surface [46, 47]. Additionally, these results demonstrate that QEGS can be used to reveal the polymer dynamics in nanocomposites and for characterising their microscopic dynamics; these insights will be important for advancing industrial materials such as tyre rubber. In the future, investigating the confinement effects of surface polymers/silica nanoparticles that are more similar to industrial tyre rubber will yield more specific information about improving tyre performance. The details of this work can be found in Ref. [21].

#### 4. Conclusions and perspectives

Quasi-elastic scattering techniques using Mössbauer gamma rays are promising approaches for revealing nanosecond and microsecond dynamics directly from the microscopic viewpoint. Currently, quasi-elastic scattering systems using the gamma rays TDI have been developed and utilised for application studies. Additionally, by using a band-width variable  $^{57}\text{Fe}$ -NBMs, we expect that the timescale of measurable dynamics will be expanded (e.g., up to sub 100 pico-second). Developing techniques that expand the timescales of measurements (i.e., between sub 100 pico-seconds and sub-microseconds), such as energy-domain quasi-elastic scattering systems combined with time-domain quasi-elastic scattering systems, is highly desirable.

Moreover, various new X-ray-based techniques are proposed for studying microscopic dynamics, based on focusing monochromators [59], or X-ray echo spectroscopy [60] or free electron lasers (e.g., four-wave mixing experiments) [61]. The combination of these new X-rays (and gamma rays)-based techniques expands the timescales of the measurements significantly (e.g., from femtoseconds to microseconds). Future studies will open new methodologies for depicting the microscopic structural dynamics of condensed matter by X-rays.



IntechOpen

## Author details

Makina Saito<sup>1\*</sup>, Toshiji Kanaya<sup>2</sup> and Ryo Mashita<sup>3</sup>

1 Institute for Integrated Radiation and Nuclear Science, Kyoto University, Kumatori, Japan

2 J-PARC, Material and Life Science Division, Institute of Material Structure Science, High Energy Accelerator Research Organization (KEK), Tokai, Japan

3 Sumitomo Rubber Industries, Ltd., Kobe, Japan

\*Address all correspondence to: msaito@rri.kyoto-u.ac.jp

## IntechOpen

© 2019 The Author(s). Licensee IntechOpen. This chapter is distributed under the terms of the Creative Commons Attribution License (<http://creativecommons.org/licenses/by/3.0>), which permits unrestricted use, distribution, and reproduction in any medium, provided the original work is properly cited. 

## References

- [1] Mössbauer RL. Kernresonanzfluoreszenz von gammastrahlung in Ir<sup>191</sup>. Zeitschrift für Physik. 1958;**151**:124-143. DOI: 10.1007/BF01344210
- [2] Greenwood NN, Gibb TC. Mössbauer Spectroscopy. London: Chapman and Hall Ltd.; 1971. 659 p. DOI: 10.1007/978-94-009-5697-1
- [3] Elliott JA, Hall HE, Bunbury DSP. Study of liquid diffusion by Mössbauer absorption and Rayleigh scattering. Proceedings of the Physical Society. 1966;**89**:595-612. DOI: 10.1088/0370-1328/89/3/315
- [4] Tischler JZ, Larson BC, Boatner LA, Alp EE, Mooney T. Time-sliced Mössbauer absorption spectroscopy using synchrotron radiation and a resonant Bragg monochromator. Journal of Applied Physics. 1996;**79**:3686-3690. DOI: 10.1063/1.361199
- [5] Masuda R, Mitsui T, Kobayashi Y, Higashitaniguchi S, Seto M. A spectrometer for Rayleigh scattering of Mössbauer radiation using synchrotron radiation. Japanese Journal of Applied Physics. 2009;**48**:120221. DOI: 10.1143/JJAP.48.120221
- [6] Baron AQR, Franz RH, Meyer A, Rüffer R, Chumakov AI, Burkel E, et al. Quasielastic scattering of synchrotron radiation by time domain interferometry. Physical Review Letters. 1997;**79**:2823-2826. DOI: 10.1103/PhysRevLett.79.2823
- [7] Balucani U, Zoppi M. Dynamics of the Liquid State. Oxford: Oxford University Press; 1994. 336 p
- [8] Champeney DC, Woodhams FWD. Investigation of molecular motions in supercooled liquids by Mössbauer scattering. The Journal of Physics B. 1968;**1**:620-631. DOI: 10.1088/0022-3700/1/4/313
- [9] Mössbauer RL. Gamma-resonance and X-ray investigations of slow motions in macromolecular systems. Hyperfine Interactions. 1987;**33**:199-222. DOI: 10.1007/BF02394109
- [10] Smirnov GV, van Bürck U, Chumakov AI, Baron AQR, Rüffer R. Synchrotron Mössbauer source. Physical Review B. 1997;**55**:5811-5815. DOI: 10.1103/PhysRevB.55.5811
- [11] Mitsui T, Masuda R, Seto M, Hirao N. Variable-bandwidth <sup>57</sup>Fe synchrotron Mössbauer source. Journal of the Physical Society of Japan. 2018;**87**:093001. DOI: 10.7566/JPSJ.87.093001
- [12] Smirnov GV, Kohn VG, Petry W. Dynamics of electron density in a medium revealed by Mössbauer time-domain interferometry. Physical Review B. 2001;**63**:144303. DOI: 10.1103/PhysRevB.63.144303
- [13] Smirnov GV, van Bürck V, Franz H, Asthalter T, Leupold O, Schreier E, et al. Nuclear  $\gamma$  resonance time-domain interferometry: Quantum beat and radiative coupling regimes compared in revealing quasielastic scattering. Physical Review B. 2006;**73**:184126. DOI: 10.1103/PhysRevB.73.184126
- [14] Saito M, Masuda R, Yoda Y, Seto M. Synchrotron radiation-based quasi-elastic scattering using time-domain interferometry with multi-line gamma rays. Scientific Reports. 2017;**7**:12558. DOI: 10.1038/s41598-017-12216-7
- [15] Saito M, Seto M, Kitao S, Kobayashi Y, Higashitaniguchi S, Kurokuzu M, et al. Development of time-domain interferometry for the study of glass formers. Journal of Physics: Conference Series. 2010;**217**:

012147-012150. DOI: 10.1088/1742-6596/217/1/012147

[16] Saito M, Kitao S, Kobayashi Y, Kurokuzu M, Yoda Y, Seto M. Slow processes in supercooled *o*-terphenyl: Relaxation and decoupling. *Physical Review Letters*. 2012;**109**:115705. DOI: 10.1103/PhysRevLett.109.115705

[17] Saito M, Kitao S, Kobayashi Y, Kurokuzu M, Yoda Y, Seto M. Slow dynamics of supercooled liquid revealed by Rayleigh scattering of Mössbauer radiation method in time domain. *Hyperfine Interactions*. 2014;**226**:629-636. DOI: 10.1007/s10751-014-1008-9

[18] Saito M, Kobayashi Y, Masuda R, Kurokuzu M, Kitao S, Yoda Y, et al. Slow dynamics in glycerol: Collective de Gennes narrowing and independent angstrom motion. *Hyperfine Interactions*. 2016;**237**:22. DOI: 10.1007/s10751-016-1243-3

[19] Yamaguchi T, Saito M, Yoshida K, Yamaguchi T, Yoda Y, Seto M. Structural relaxation and viscoelasticity of a higher alcohol with mesoscopic structure. *Journal of Physical Chemistry Letters*. 2018;**9**:298-301. DOI: 10.1021/acs.jpcllett.7b02907

[20] Kanaya T, Inoue R, Saito M, Seto M, Yoda Y. Relaxation transition in glass-forming polybutadiene as revealed by nuclear resonance X-ray scattering. *The Journal of Chemical Physics*. 2014;**140**:144906. DOI: 10.1063/1.4869541

[21] Saito M, Mashita R, Masuda R, Kishimoto H, Yoda Y, Seto M. Effect of silica nanoparticle filler on microscopic polymer  $\alpha$ -relaxation dynamics. *Hyperfine Interactions*. 2017;**238**:99. DOI: 10.1007/s10751-017-1466-y

[22] Saito M, Seto M, Kitao S, Kobayashi Y, Higashitaniguchi S, Kurokuzu M, et al. Development of 151-Eu time-domain interferometry and its application for the study of slow

dynamics in ionic liquids. *Applied Physics Express*. 2009;**2**:026502. DOI: 10.1143/APEX.2.026502

[23] Kaisermayr M, Sepiol B, Thiess H, Vogl G, Alp EE, Sturhahn W. Time-domain interferometry using synchrotron radiation applied to diffusion in ordered alloys. *The European Physical Journal B*. 2001;**20**:335-341. DOI: 10.1007/s100510170254

[24] Saito M, Seto M, Kitao S, Kobayashi Y, Kurokuzu M, Yamamoto J, et al. Small and large angle quasi-elastic scattering experiments by using nuclear resonant scattering on typical and amphiphilic liquid crystals. *Journal of the Physical Society of Japan*. 2012;**81**:023001. DOI: 10.1143/JPSJ.81.023001

[25] Debenedetti PG, Stillinger FK. Supercooled liquids and the glass transition. *Nature*. 2001;**410**:259-267. DOI: 10.1038/35065704

[26] Angell CA. Relaxation in glassforming liquids and amorphous solids. *The Journal of Applied Physics*. 2000;**88**:3113-3157. DOI: 10.1063/1.1286035

[27] Ngai KL. *Relaxation and Diffusion in Complex Systems*. Berlin: Springer; 2011. 835 p. DOI: 10.1007/978-1-4419-7649-9

[28] Angell CA. Relaxation in liquids, polymers and plastic crystals - strong/fragile patterns and problems. *Journal of Non-Crystalline Solids*. 1991;**131-133**:13-31. DOI: 10.1016/0022-3093(91)90266-9

[29] Novikov VN, Sokolov AP. Universality of the dynamic crossover in glass-forming liquids: A “magic” relaxation time. *Physical Review E*. 2003;**67**:031507. DOI: 10.1103/PhysRevE.67.031507

[30] Johari GP, Goldstein M. Viscous liquids and the glass transition. II. Secondary relaxations in glasses of rigid molecules. *The Journal of Chemical*

Physics. 1970;**53**:2372-2388. DOI:  
 10.1063/1.1674335

[31] Hansen C, Stickel F, Berger T, Richert R, Fischer EW. Dynamics of glass-forming liquids. III. Comparing the dielectric  $\alpha$ - and  $\beta$ -relaxation of 1-propanol and o-terphenyl. The Journal of Chemical Physics. 1997;**107**: 1086-1093. DOI: 10.1063/1.474456

[32] Fujara F, Geil B, Sillescu H, Fleischer G. Translational and rotational diffusion in supercooled orthoterphenyl close to the glass transition. Zeitschrift für Physik B. 1992;**88**:195-204. DOI: 10.1007/BF01323572

[33] Steffen W, Patkowski A, Gläser H, Meier G, Fischer EW. Depolarized-light-scattering study of orthoterphenyl and comparison with the mode-coupling model. Physical Review E. 1994;**49**: 2992-3002. DOI: 10.1103/PhysRevE.49.2992

[34] Petry W, Bartsch E, Fujara F, Kiebel M, Sillescu H, Farago B. Dynamic anomaly in the glass transition region of orthoterphenyl. Zeitschrift für Physik B. 1991;**83**:175-184. DOI: 10.1007/BF01309415

[35] Rössler E, Warschewske U, Eiermann P, Sokolov AP, Quitmann D. Dynamic anomaly in the glass transition region of orthoterphenyl. Journal of Non-Crystalline Solids. 1994;**172-174**:113-125. DOI: 10.1016/0022-3093(94)90424-3

[36] Johari GP. Localized molecular motions of  $\beta$ -relaxation and its energy landscape. Journal of Non-Crystalline Solids. 2002;**307**:317-325. DOI: 10.1016/S0022-3093(02)01491-6

[37] Williams G, Watts DC. Molecular aspects of multiple dielectric relaxation process in solid polymers. Advances in Polymer Science. 1979;**33**:59-92. DOI: 10.1007/3-540-09456-3\_3

[38] Vogel M, Rössler E. On the nature of slow  $\alpha$ -process in simple glass formers:

A 2H NMR study. The Journal of Physical Chemistry. B. 2000;**104**: 4285-4287. DOI: 10.1021/jp9942466

[39] Langer J. The mysterious glass transition. Physics Today. 2007;**60**:8-9. DOI: 10.1063/1.2711621

[40] Kulik AS, Beckham HW, Schmidt-Rohr K, Radloff D, Pawelzik UP, Boeffel C, et al. Coupling of  $\alpha$  and  $\beta$  processes in poly(ethyl methacrylate) investigated by multidimensional NMR. Macromolecules. 1994;**27**:4746-4754. DOI: 10.1021/ma00095a015

[41] Garwe F, Schönhals A, Lockwenz H, Beiner M, Schöter K, Donth E. Influence of cooperative  $\alpha$  dynamics on local  $\beta$  relaxation during the development of the dynamic glass transition in poly(*n*-alkyl methacrylate)s. Macromolecules. 1996;**29**:247-253. DOI: 10.1021/ma9506142

[42] Richter D, Frick B, Farago B. Neutron-spin-echo investigation on the dynamics of polybutadiene near the glass transition. Physical Review Letters. 1988;**61**:2465-2468. DOI: 10.1103/PhysRevLett.61.2465

[43] Richter D, Zorn R, Farago B, Frick B, Fetters LJ. Decoupling of time scales of motion in polybutadiene close to the glass transition. Physical Review Letters. 1992;**68**:71-74. DOI: 10.1103/PhysRevLett.68.71

[44] Arbe A, Buchenau U, Willner L, Richter D, Farago B, Colmenero J. Study of the dynamic structure factor in the  $\beta$  relaxation regime of polybutadiene. Physical Review Letters. 1996;**76**: 1872-1875. DOI: 10.1103/PhysRevLett.76.1872

[45] Chong SH. Connections of activated hopping processes with the breakdown of the stokes-Einstein relation and with aspects of dynamical heterogeneities. Physics Review. 2008;**E 78**:041501. DOI: 10.1103/PhysRevE.78.041501



- [46] Mai YW, Yu ZZ. Polymer Nanocomposites. Cambridge: Woodhead Publishing; 2006. 608 p
- [47] Jancar J, Douglas JF, Starr FW, Kumar SK, Cassagnau P, Lesser AJ, et al. Current issues in research on structure–property relationships in polymer nanocomposites. *Polymer*. 2010;**51**: 3321–3343. DOI: 10.1016/j.polymer.2010.04.074
- [48] Arrighi V, Higgins JS, Burgess AN, Floudas G. Local dynamics of poly (dimethyl siloxane) in the presence of reinforcing filler particles. *Polymer*. 1998;**39**:6369–6376. DOI: 10.1016/S0032-3861(98)00139-6
- [49] Gagliardi S, Arrighi V, Ferguson R, Telling MTF. Restricted dynamics in polymer-filler systems. *Physica B*. 2001; **301**:110–114. DOI: 10.1016/S0921-4526 (01)00520-8
- [50] Nusser K, Schneider GJ, Richter D. Microscopic origin of the terminal relaxation time in polymer nanocomposites: An experimental precedent. *Soft Matter*. 2011;**7**: 7988–7991. DOI: 10.1039/C1SM05555K
- [51] Schneider GJ, Nusser K, Willner L, Falus P, Richter D. Dynamics of entangled chains in polymer nanocomposites. *Macromolecules*. 2011; **44**:5857–5860. DOI: 10.1021/ma200899y
- [52] Roh JH, Tyagi M, Hogan TE, Roland CM. Space-dependent dynamics in 1,4-polybutadiene nanocomposite. *Macromolecules*. 2013;**46**:6667–6669. DOI: 10.1021/ma401597r
- [53] Roh JH, Tyagi M, Hogan TE, Roland CM. Effect of binding to carbon black on the dynamics of 1,4-polybutadiene. *The Journal of Chemical Physics*. 2013;**139**:134905. DOI: 10.1063/1.4822476
- [54] Glomann T, Hamm A, Allgaier J, Hubner EG, Radulescu A, Farago B, et al. A microscopic view on the large scale chain dynamics in nanocomposites with attractive interactions. *Soft Matter*. 2013;**9**:10559–10571. DOI: 10.1039/C3SM51194D
- [55] Glomann T, Schneider GJ, Allgaier J, Radulescu A, Lohstroh W, Farago B, et al. Microscopic dynamics of polyethylene glycol chains interacting with silica nanoparticles. *Physical Review Letters*. 2013;**110**:178001. DOI: 10.1103/PhysRevLett.110.178001
- [56] Schneider GJ, Nusser K, Neueder S, Brodeck M, Willner L, Farago B, et al. Anomalous chain diffusion in unentangled model polymer nanocomposites. *Soft Matter*. 2013;**9**: 4336–4348. DOI: 10.1039/C3SM27886G
- [57] Guo H, Bourret G, Lennox RB, Sutton M, Harden JL, Leheny RL. Entanglement-controlled subdiffusion of nanoparticles within concentrated polymer solutions. *Physical Review Letters*. 2012;**109**:055901. DOI: 10.1103/PhysRevLett.109.055901
- [58] Deegan RD, Nagel SR. Dielectric susceptibility measurements of the primary and secondary relaxation in polybutadiene. *Physical Review B*. 1995; **52**:5653. DOI: 10.1103/PhysRevB.52.5653
- [59] Kohn VG, Chumakov AI, Rüffer R. Wave theory of focusing monochromator of synchrotron radiation. *Journal of Synchrotron Radiation*. 2009;**16**:635–641. DOI: 10.1107/S090904950902319X
- [60] Shvyd'ko Y. X-ray echo spectroscopy. *Physical Review Letters*. 2016;**116**:080801. DOI: 10.1103/PhysRevLett.116.080801
- [61] Bencivenga F, Cucini R, Capotondi F, Battistoni A, Mincigrucci R, Giangrisostomi E, et al. Four-wave mixing experiments with extreme ultraviolet transient gratings. *Nature*. 2015;**520**:205–208. DOI: 10.1038/nature14341